Dynamic Modeling and Feasibility Analysis of a Solid-State Transformer Based Power Distribution System

Md Tanvir Arafat Khan Alireza Afiat Milani Aranya Chakrabortty Iqbal Husain
Electrical and Computer Engineering Department
FREEDM Systems Center
North Carolina State University
Raleigh, NC, USA
mtkhan@ncsu.edu

***Abstract*— This paper presents a comprehensive state-space dynamic model of a future power distribution system for plug-and-play interface of distributed renewable energy resources and distributed energy storage devices. The system, called the FREEDM system, comprises of multiple solid-state transformers (SSTs), and load, generation and storage connected to each SST in a distributed network. The system allows for high penetration of renewable generation with energy storage at the distribution level. A physics based 70th order state-space average model is first developed considering the physical and controller properties of a single-SST FREEDM system along with its distribution components. This fundamental model is then extended to build a multi-SST FREEDM system for feasibility and dynamics behavior analysis of the entire system which is essential to ensure system power balance. The full average model with multiple SSTs has been incorporated in an IEEE 34 bus distribution testbed for a scaled analysis of the system.**

I. INTRODUCTION

The Future Renewable Electric Energy Delivery and Management (FREEDM) power distribution system is designed to facilitate distributed renewable generation and energy storage integration and plug-and-play interface of these components. The system consists of one or more solid-state transformers (SSTs) enabled with communication which serve as an energy router that allow flexible energy sharing among consumers in a residential and/or industrial distribution system [1]. The one-node FREEDM system consists of a single-SST, a DC energy cell and an AC energy cell on the low voltage side of the distribution system [2]. Each AC or DC energy cell consists of Distributed Renewable Energy Resources (DRERs), Distributed Energy Storage Devices (DESDs) and local loads. Fig. 1 shows a two-node FREEDM system with all the distribution components in the energy cells. The renewable generation sources and the storage devices are enabled to be plug-and-play types with the power electronic converter stage between these devices and the system nodes. Each SST with its built-in intelligence and communication features serves as an energy management unit, or in other words as an energy router, to enable integration of energy cell components with the traditional grid [1, 2, and 3].

The SST is a power electronics based device that can provide efficient operation with much smaller size and lower mass compared to an iron core traditional 60Hz distribution transformer [3, 4, and 5]. The advancements in power electronics and converter control techniques make it possible to utilize the SST to buffer the Medium Voltage (MV) grid from the Low Voltage (LV) distribution side where local generations, storages and loads are located. SST improves the performance of the power system by incorporating power quality features such as power factor correction, instantaneous voltage regulation, voltage sag tolerance, and harmonic isolation at the distribution level (residential users and industry customers) [1, 6]. The SST with its intelligence sharing feature with other SSTs in the system can improve system reliability while prioritizing the usage of maximum possible green energy [6, 7]. Prior research focused on developing simplified models of single-SST without considering the renewable generation and storage components and their physical constraints or interactions among the SSTs [8, 9, 10, and 11]. A comprehensive system level study relating the operational constraints introduced by the physical parameters were not addressed previously. Failures were observed in prior SST based distribution system analysis, but the fundamental reasons for the failures were not unearthed [12]. The primary contributions of the paper are twofold: First, the development of a physics based 70th order state-space average model considering the physical and controller properties of a single-SST FREEDM system along with its distribution level energy cell components; second, use the fundamental model to build a multi-SST FREEDM system for feasibility and dynamics behavior analysis of the entire

system. Feasibility analysis addresses the power balance of the multi-SST system which is a necessary condition for system stability. In addition, including the dynamic features of PV, wind and storage with the dynamic characteristics of the SST is essential for a comprehensive system analysis. The full average model with multiple SSTs has also been incorporated in an IEEE 34 bus distribution testbed for a scaled analysis of the system.

Feasibility and equilibrium analysis enables us to evaluate system operational bounds of a multi-SST distribution system due to the coupling and interaction among various system components. The developed multi-SST model is used to find the feasible operating bounds of the system. System power balance addressed through the feasibility or equilibrium analysis is a necessary condition for system stability for a given power flow condition. If an infeasible operating point is chosen for the system, no controller will be able to maintain system operation. It is to be noted here that controller design to avoid unstable operating points due to harmonic resonance among multiple SSTs is also critical which needs to be addressed after ensuring system feasibility. This paper focuses on model based analysis to ensure feasible operation of all SSTs in the system.

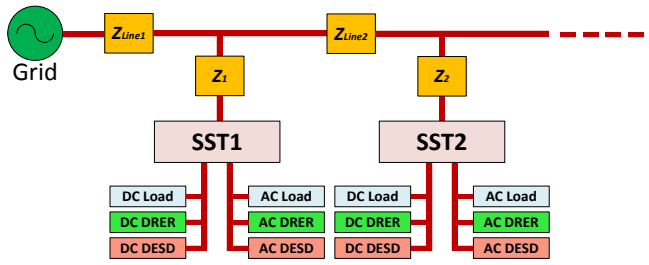

Figure 1. One node FREEDM system model.

II. AVERAGE MODEL OF THE FREEDM SYSTEM

The FREEDM system consists of SST, DRER, DESD and local loads that makes its overall dynamics nonlinear in nature. The SST has three power electronics stages to interface the MVAC in the distribution grid with both LVDC and LVAC. These three conversion stages are: Rectifier, Dual Active Bridge (DAB) and Inverter as shown in Fig. 2. The rectifier stage converts MVAC power into MVDC power which is then processed by the DAB to convert the MVDC output into lower voltage levels. The DAB is essentially a DC-DC converter with a high frequency transformer. The inverter converts LVDC into LVAC for the AC energy cell applications. Existing modeling approach is based on single-SST configurations without the energy cell components and the controllers were developed based on the assumption of existence of an equilibrium point [2, 8, and 9]. This work presents an end-to-end comprehensive mathematical model capturing all the nonlinear, and sometimes non-smooth, dynamic phenomena triggered by different types of switching command, and disturbances within a multi-SST based FREEDM system. The modeling process starts with building sub-system state-space models, such as those for SST, Wind DRER, PV DRER and DESD. The sub-system models are then integrated to build the comprehensive FREEDM system model. The component states and the associated controller states are also separated such that the plant model and the controller model can be developed and upgraded individually. In Fig. 2, all the parameters and physical states are shown by a_i and x_i, respectively. PI controller states are denoted by ξ_i; and d_i's are the output of the controllers. DAB output current is denoted by I_{DAB}, rectifier net output power is presented by P_{rec}, while L_{DC} and L_{AC} represent the net load of DC and AC energy cells (generation sources, energy storage and local loads), respectively.

The time-scales of evolution of the different states, however, are sharply different ranging from 10^{-3} microseconds to 0.1 seconds within the SST. Singular perturbation techniques have been applied to reduce the model order, and represent it in a more tractable form. Singular perturbation method separates the dynamic system into slow and fast variables that allow the simplification of the rectifier model by eliminating the states that have no effects on system performance [13]. Total system states have been reduced from more than hundreds for the full FREEDM system by utilizing the model reduction technique which made the system analysis manageable. The final order of the simplified derived model, including all internal controller states, is 70.

A. SST - Rectifier Model and Controllers

The rectifier is the connection point of the SST, and more generally the FREEDM system to the grid. The modeled rectifier has an LCL filter at the front end which is simplified to represent an L-rectifier through model reduction. In a dual loop controller, the rectifier output voltage is controlled in the outer loop that generates the *d*-axis current reference for controlling the i_d-component of the SST input current in the inner loop. Current reference can be set to zero for unity power factor in the *q*-axis controller that controls the reactive power flow.

Fig. 2 shows the simplified circuit diagram of the rectifier and the equations (1)-(8) present the rectifier physical states, controller states and controller output where y_1, y_2, $x_1$and x_2 represent *d* and *q*-axes grid voltages and currents, respectively. All the parameters and states are listed in table 1.

$$\dot{x}_1 = -\frac{a_2}{a_1}x_1 + \omega_1 x_2 + \frac{1}{a_1}d_1 x_3 - \frac{1}{a_1}y_1 \quad (1)$$

$$\dot{x}_2 = -\omega_1 x_1 - \frac{a_2}{a_1}x_2 + \frac{1}{a_1}d_2 x_3 - \frac{1}{a_1}y_2 \quad (2)$$

$$\dot{x}_3 = -\frac{1}{a_3}d_a x_a - \frac{P_{rec}}{a_3 x_3} \quad (3)$$

$$\dot{\xi}_1 = r_1 - x_3 \quad (4)$$

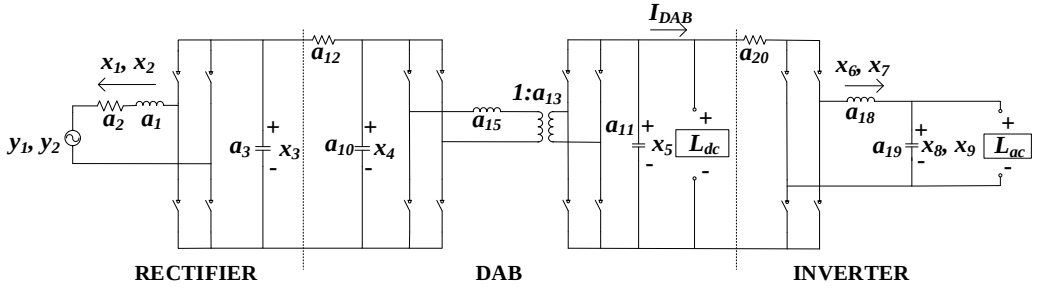

Figure 2. Solid-state transformer circuit model.

$$\dot{\xi}_2 = a_4(r_1 - x_3) + a_5\xi_1 - x_1 \quad (5)$$
$$\dot{\xi}_3 = q_1 - x_2 \quad (6)$$
$$d_1 = a_6(a_4(r_1 - x_3) + a_5\xi_1 - x_1) + a_7\xi_2 \quad (7)$$
$$d_2 = a_8(q_1 - x_2) + a_9\xi_3 \quad (8)$$
$$d_a = d_1\cos(\theta) + d_2\sin(\theta) \quad (9)$$
$$x_a = x_1\cos(\theta) + x_2\sin(\theta) \quad (10)$$

d_a and x_a can be found using equations (9-10) through single phase $\alpha\beta$- dq modeling and the phase output (θ) from the phase locked loop (PLL) block. PLL synchronizes with the input voltage of the SST such that accurate phase of the AC voltage can be detected. Substituting (9)-(10) in (3), second harmonic terms will appear in (3) that represents the second harmonic oscillation superimposed on the steady state value of each signal. It is important to capture this dynamic variation of the AC side in the output DC voltage of the rectifier which was not reported earlier [8, 14]. The SST control loops are given in Fig. 3 in the *d*-*q* domain; the parameter values are the same as those in the hardware SST built for the FREEDM system [15]. The controller gains for different stages of the SST are chosen based on the eigenvalue analysis; the eigenvalue plots with the selected gains are shown in Fig. 4.

B. SST - DAB Model and Controllers

The DAB consists of two full bridges and a high frequency transformer in between these bridges. In order to be able to transfer the power from the first bridge to the second one, phase difference must exist between the switching of these bridges. The states of the system are input and output capacitor voltages and inductor current. However, the system can be divided into a slow-varying system and a fast-varying system since the capacitor voltage changes are much slower compared to the changes in inductor current [16]. The two-dimensional representation of the DAB converter is obtained by linearly representing the fast varying inductor current in each sub-interval and applying the state-space averaging method. Equations (11)-(14) provide the final state equations for DAB along with the controller output.

$$\dot{x}_4 = +\frac{1}{a_{10}a_{12}}x_3 - \frac{1}{a_{10}a_{12}}x_4 - \frac{d_3(1-d_3)a_{13}}{2a_{10}a_{14}a_{15}}x_5 \quad (11)$$

$$\dot{x}_5 = \frac{d_3(1-d_3)a_{13}}{2a_{11}a_{14}a_{15}}x_4 - \frac{1}{a_{11}L_{DC}}x_5 \quad (12)$$
$$\dot{\xi}_4 = r_2 - x_5 \quad (13)$$
$$d_3 = a_{16}(r_2 - x_5) + a_{17}\xi_4 \quad (14)$$

C. SST - Inverter Model and Controllers

In the inverter stage, the AC inverter controls the magnitude of the output side AC voltage in the *dq* reference frame to interface with the AC energy cell. An inner current loop can be added to track the voltage references faster. The inverter circuit diagram is shown in Fig. 2. Inverter state equations, controller states and outputs are given in equations (15)-(22), where x_6, x_7, x_8 and x_9 represent *d* and *q* -axes inverter output currents and voltages, respectively.

$$\dot{x}_6 = \frac{1}{a_{18}}d_4x_5 - \frac{a_{20}}{a_{18}}x_6 + \omega_2x_7 - \frac{1}{a_{18}}x_8 \quad (15)$$
$$\dot{x}_7 = \frac{1}{a_{18}}d_5x_5 - \omega_2x_6 - \frac{a_{20}}{a_{18}}x_7 - \frac{1}{a_{18}}x_9 \quad (16)$$
$$\dot{x}_8 = \frac{1}{a_{19}}x_6 - \frac{1}{a_{19}L_{AC}}x_8 + \omega_2x_9 \quad (17)$$
$$\dot{x}_9 = \frac{1}{a_{19}}x_7 - \omega_2x_8 - \frac{1}{a_{19}L_{AC}}x_9 \quad (18)$$
$$\dot{\xi}_5 = r_3 - x_8 \quad (19)$$
$$\dot{\xi}_6 = -x_9 \quad (20)$$
$$d_4 = a_{21}(y_3 - x_8) + a_{22}\xi_5 \quad (21)$$
$$d_5 = a_{23}(y_4 - x_9) + a_{24}\xi_6 \quad (22)$$

D. DRER Model and Controllers

Both the DC and AC energy cells have similar components on the LV side consisting of a PV DRER, Wind DRER, one DESD and a load. The difference in the DC and AC energy cells is in the power electronics interface circuits connecting them to the DC and AC buses. Each component along with its coupling on both the DC and AC energy cells have been modeled separately to capture the detailed physical characteristics which were missing in previous studies. Both PV and Wind DRERs have been considered for generality in the FREEDM system, although in reality, only one type is expected to be present in an energy cell. The physics based PV model has been focused in this paper; where the parameters of the nonlinear *I-V* equation are found by adjusting the curve at three points: open circuit, maximum power, and short circuit [17, 18].

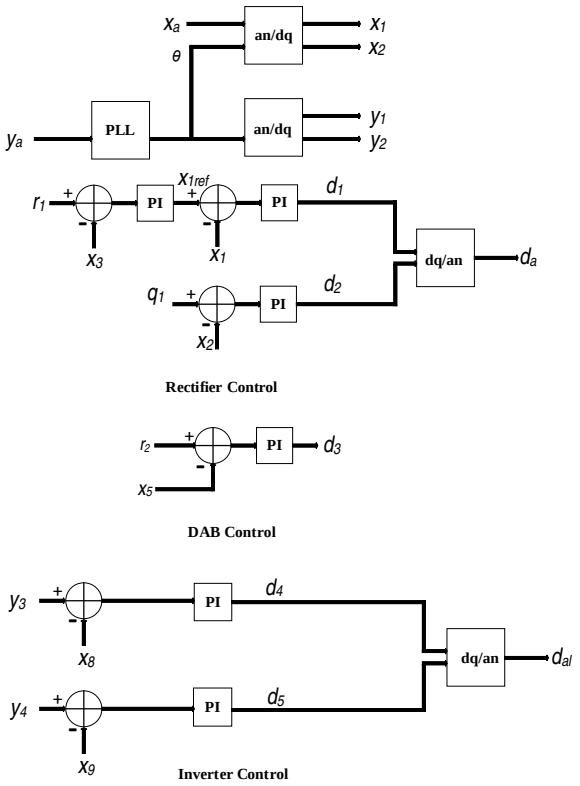

Figure 3. SST control structure with its internal control loops.

The rectifier and inverter average models of the DRERs are matched with the average model of SST's rectifier and inverter to maintain consistency in modeling. Mathematical models and interface circuits of the PV DRERs for both the AC and DC energy cells are provided in the next paragraph. Wind DRER is also developed with a total of 26 system and controller states in DC and AC energy cells in a similar manner as that of the PV DRER, which is not presented to avoid repetition. Fig. 5 presents the PV DRER interface circuit for AC energy cells. Boost converter is coupled with rectifier circuit to convert the lower DC voltage of the PV system to lower AC voltage. DRER circuit is directly connected to the AC bus through the interface circuit. Mathematical model for the interface is also developed and shown in equations (23)-(35). While the SST local controller regulates the AC bus voltages, the control objective of PV DRER model is to operate at Maximum Power Point (MPP) through control of the interface circuit.

$$\dot{x}_{10} = \frac{1}{a_{25}} x_{11} - \frac{1-d_6}{a_{25}} x_{12} \tag{23}$$
$$\dot{x}_{11} = -\frac{1}{a_{26}} x_{10} + \frac{1}{a_{26}} \frac{r_6}{x_{11}} \tag{24}$$
$$\dot{x}_{12} = \frac{1-d_6}{a_{27}} x_{10} - \frac{1}{a_{27}a_{28}} x_{12} + \frac{1}{a_{27}a_{28}} x_{15} \tag{25}$$
$$\dot{x}_{13} = -\frac{1}{a_{31}} x_8 - \frac{a_{33}}{a_{31}} x_{13} + \omega_2 x_{14} + \frac{1}{a_{31}} d_7 x_{15} \tag{26}$$
$$\dot{x}_{14} = -\frac{1}{a_{31}} x_9 - \omega_2 x_{13} - \frac{a_{33}}{a_{31}} x_{14} + \frac{1}{a_{31}} d_8 x_{15} \tag{27}$$
$$\dot{x}_{15} = -\frac{1}{2a_{32}} d_7 x_{13} - \frac{1}{2a_{32}} d_8 x_{14} - \frac{1}{a_{32}} \frac{u_2}{x_{15}} \tag{28}$$
$$\dot{\xi}_7 = r_5 - x_{11} \tag{29}$$
$$\dot{\xi}_8 = r_4 - x_{15} \tag{30}$$
$$\dot{\xi}_9 = a_{34}(r_3 - x_{15}) + a_{35}\xi_8 - x_{13} \tag{31}$$
$$\dot{\xi}_{10} = -x_{16} \tag{32}$$
$$d_6 = a_{36}(r_5 - x_{11}) + a_{37}\xi_7 \tag{33}$$
$$d_7 = a_{38}(a_{34}(r_4 - x_{15}) + a_{35}\xi_8 - x_{13}) + a_{39}\xi_9 \tag{34}$$
$$d_8 = -a_{40}x_{16} + a_{41}\xi_{10} \tag{35}$$

The PV modules are connected to LVDC bus through a boost converter to amplify the panel voltage as shown in the PV DRER interface circuit in Fig. 6. Based on voltage level of the panels, other DC-DC converters can also be coupled to the LVDC bus. Boost converter handles the MPP tracking algorithm for the PV DRER as the DC bus voltage is regulated by the SST DAB local controller. Mathematical model for the interface is also developed and shown in equations (36)-(40).

$$\dot{x}_{22} = \frac{1}{a_{42}} x_{23} - \frac{(1-d_{11})}{a_{42}} x_{24} \tag{36}$$
$$\dot{x}_{23} = -\frac{1}{a_{43}} x_{22} + \frac{r_8}{a_{43}x_{23}} \tag{37}$$
$$\dot{x}_{24} = \frac{(1-d_{11})}{a_{44}} x_{22} - \frac{1}{a_{44}a_{45}} x_{24} + \frac{1}{a_{44}a_{45}} x_5 \tag{38}$$
$$\dot{\xi}_{13} = r_7 - x_{23} \tag{39}$$
$$d_{11} = a_{46}(r_7 - x_{23}) + a_{47}\xi_{13} \tag{40}$$

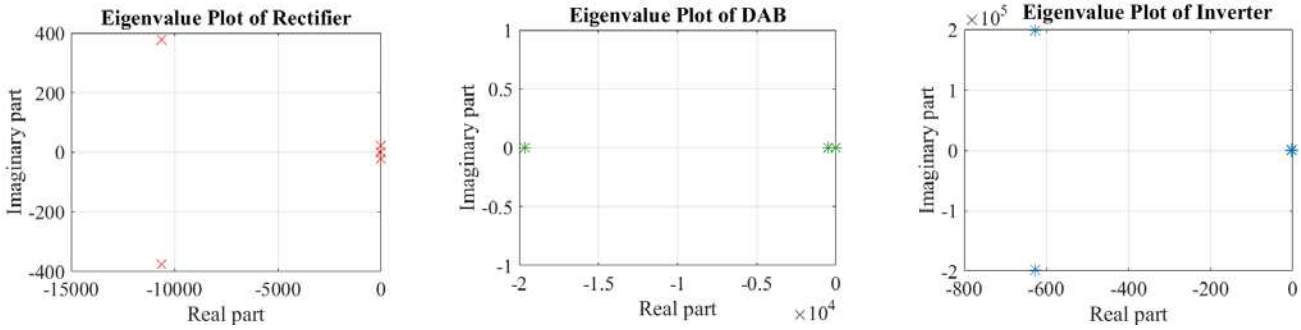

Figure 4: Eigenvalue plots of the SST stages.

Table 1: System and controller states, references and parameters list for FREEDM system.

System and Controller States							
x_1	Rectifier d-axis inductor current	x_7	Inverter q-axis inductor current	$x_{25} - x_{30}$	DC DESD interface converter states	ξ_{13}	DC DRER interface converter controller state
x_2	Rectifier q-axis inductor current	x_8	Inverter d-axis capacitor voltage	$\xi_1 - \xi_3$	Rectifier controller states	ξ_{14}	DC DESD interface converter controller states
x_3	Rectifier capacitor voltage	x_9	Inverter q-axis capacitor voltage	ξ_4	DAB controller state		
x_4	DAB input capacitor voltage	$x_{10} - x_{15}$	AC DRER interface converter states	$\xi_5 - \xi_6$	Inverter controller states		
x_5	DAB output capacitor voltage	$x_{16} - x_{21}$	AC DESD interface converter system states	$\xi_7 - \xi_{10}$	AC DRER interface converter controller states		
x_6	Inverter d-axis inductor current	$x_{22} - x_{24}$	DC DRER interface converter states	$\xi_7 - \xi_{10}$	AC DESD interface converter controller states		
System Parameters							
a_1	Rectifier filter inductor	a_{11}	DAB output capacitor	a_{19}	Inverter filter capacitor	$a_{46} - a_{47}$	DC DRER interface converter controller gains
a_2	Rectifier filter resistor	a_{12}	DAB input resistor	a_{20}	Inverter input filter resistor	$a_{48} - a_{57}$	AC DESD physical parameters
a_3	Rectifier capacitor	a_{13}	Transformer turns ratio	a_{21}, a_{22}	Inverter d-axis gains of controller	$a_{58} - a_{61}$	AC DESD interface converter controller gains
a_4, a_5	Rectifier gains of voltage controller	a_{14}	Transformer switching frequency	a_{23}, a_{24}	Inverter q-axis gains of controller	$a_{62} - a_{75}$	DC DESD physical parameters
a_6, a_7	Rectifier d-axis gains of controller	a_{15}	Transformer inductor	$a_{25} - a_{33}$	AC DRER physical parameters	$a_{76} - a_{77}$	DC DESD interface converter controller gains
a_8, a_9	Rectifier q-axis gains of controller	a_{16}, a_{17}	DAB PI controller gains	$a_{34} - a_{41}$	AC DRER interface converter controller gains		
a_{10}	DAB input capacitor	a_{18}	Inverter filter inductor	$a_{42} - a_{45}$	DC DRER physical parameters		
System References							
ω_1	Rectifier frequency	L_{AC}	Inverter net output load (Ohms)	r_3	Inverter d-axis reference voltage	r_7	DC DRER maximum power point voltage
ω_2	Inverter frequency	q_1	Rectifier q-axis reference current	r_4	AC DRER converter reference voltage	r_8	DC DRER maximum power point power
P_{rec}	Rectifier net output power	r_1	Rectifier output reference voltage	r_5	AC DRER maximum power point voltage	r_9	AC DESD charging/ discharging current reference
L_{DC}	DAB net output load (Ohms)	r_2	DAB output reference voltage	r_6	AC DRER maximum power point power	r_{10}	DC DESD charging/ discharging current reference
Control Outputs							
d_1	Rectifier d-axis converter duty cycle	d_4	Inverter d-axis converter duty cycle	$d_6 - d_8$	AC DRER converter duty cycles	d_{11}	DC DRER converter duty cycle
d_2	Rectifier q-axis converter duty cycle	d_5	Inverter q-axis converter duty cycle	$d_9 - d_{10}$	AC DESD converter duty cycles	d_{12}	DC DESD converter duty cycle
d_3	DAB converter duty cycle						

E. DESD Model and Controllers

The power electronics based interface with bi-directional capability controls the DESD charging/discharging voltage and current for power and energy management of the system. The charging voltage of DESD is typically lower than the DC bus voltage, and hence, a good choice for this interface circuit is a buck converter for the DC energy cell and an inverter coupled buck converter for AC energy cell.

However, to allow flexibility in choosing the voltage rating of the battery, a bidirectional buck-boost converter for DC DESD and an inverter coupled with a buck-boost converter have been used for AC DESD. Power electronics interface circuits for AC DESD and DC DESD are shown in Fig. 7 and Fig. 8, respectively. Mathematical models of the AC DESD are given in equations (41)-(50). DESD model for the FREEDM system has utilized the detailed storage modeling to capture all the transients [19, 20].

$$\dot{x}_{16} = -\frac{1}{a_{48}} x_8 - \frac{a_{50}}{a_{48}} x_{16} + \omega_2 x_{17} + \frac{1}{a_{50}} d_9 x_{18} \tag{41}$$

$$\dot{x}_{17} = -\frac{1}{a_{48}} x_9 - \omega_2 x_{16} - \frac{a_{50}}{a_{48}} x_{17} + \frac{1}{a_{48}} d_{10} x_{18} \tag{42}$$

$$\dot{x}_{18} = -\frac{1}{2a_{49}} d_9 x_{16} - \frac{1}{2a_{49}} d_{10} x_{17} - \frac{1}{a_{49}a_{51}} x_{18} + \frac{1}{a_{49}a_{51}} * (V_{oc} + x_{20} + x_{21} - x_{18}) \tag{43}$$

$$\dot{x}_{19} = -\frac{1}{a_{52}a_{53}} x_{19} + \frac{1}{a_{52}(a_{51} + a_{50})} * (V_{oc} + x_{20} + x_{21} - x_{18}) \tag{44}$$

$$\dot{x}_{20} = -\frac{1}{a_{54}a_{55}}x_{20} + \frac{1}{a_{54}(a_{51}+a_{50})} * (V_{oc} + x_{20} + x_{21} - x_{18}) \quad (45)$$

$$\dot{x}_{21} = -\frac{1}{a_{56}a_{57}}x_{21} + \frac{1}{a_{56}(a_{51}+a_{50})} * (V_{oc} + x_{20} + x_{21} - x_{18}) \quad (46)$$

$$\dot{\xi}_{11} = r_9 - x_{16} \quad (47)$$

$$\dot{\xi}_{12} = -x_{17} \quad (48)$$

$$d_9 = a_{58}(r_9 - x_{16}) + a_{59}\xi_{11} \quad (49)$$

$$d_{10} = -a_{60}a_{17} + a_{61}\xi_{12} \quad (50)$$

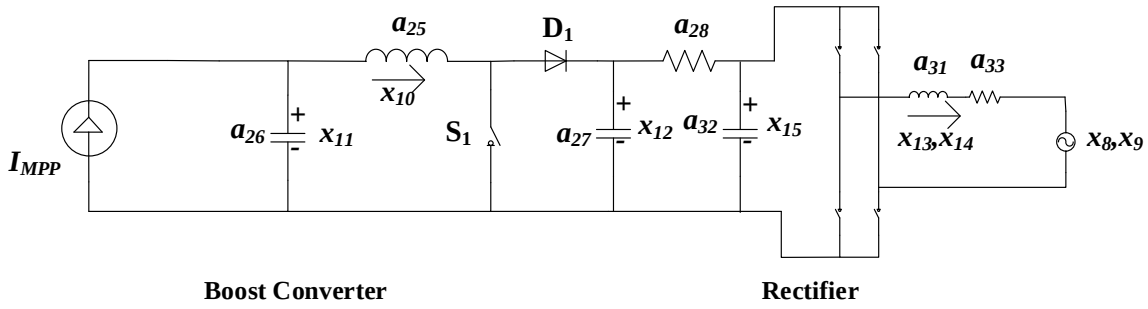

Figure 5: PV DRER, Boost converter and rectifier for PV AC interface.

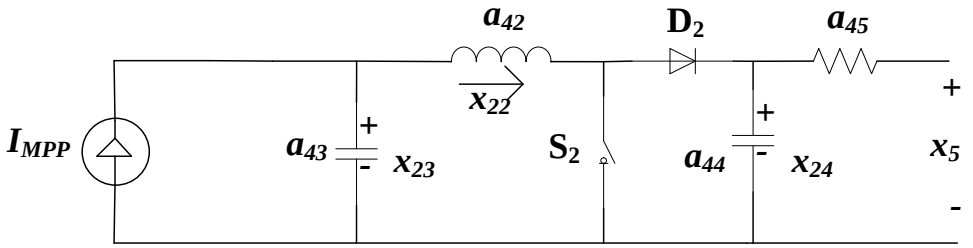

Figure 6: PV DRER and Boost converter for PV DC interface.

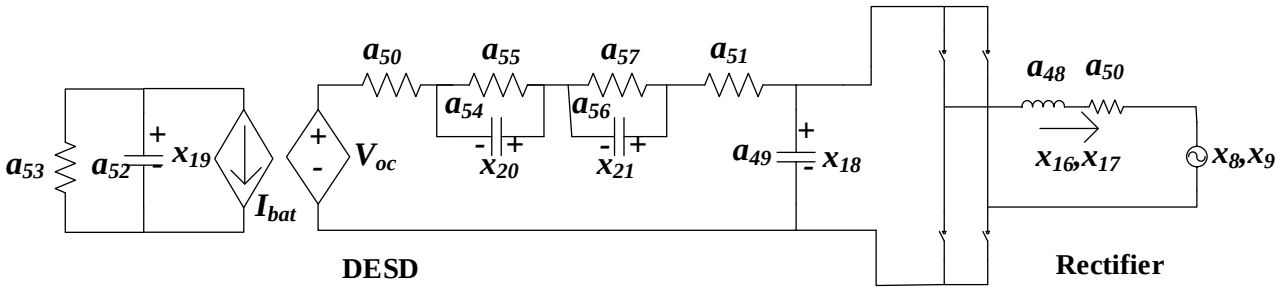

Figure 7: DESD and Rectifier circuit for AC DESD average model.

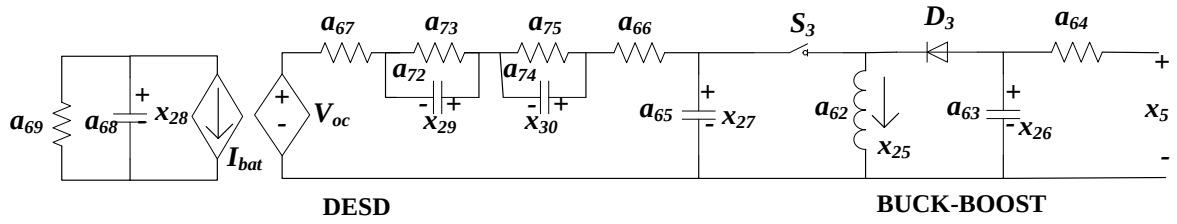

Figure 8: DESD and Buck-Boost circuit for DC DESD average model.

DC DESD is directly connected to the DC bus and so the rectifier stage is not required. Mathematical models for DC DESD with Buck-Boost converter are provided in equations (51)-(58). Battery State-of-charge (SOC) is included in the storage model defining it as the voltage across the equivalent storage capacitors a_{52} and a_{68} for the AC and DC DESDs, respectively.

$$\dot{x}_{25} = \frac{(1-d_{12})}{a_{62}} x_{26} + \frac{d_{12}}{a_{62}} x_{27} \quad (51)$$

$$\dot{x}_{26} = \frac{1}{a_{63}a_{64}} x_5 - \frac{(1-d_{12})}{a_{63}} x_{25} - \frac{1}{a_{63}a_{64}} x_{26} \quad (52)$$

$$\dot{x}_{27} = -\frac{d_{12}}{a_{65}} x_{25} + \frac{(1-d_{12})}{a_{65}(a_{66}+a_{67})} * (V_{oc} + x_{29} + x_{30} - x_{27}) \quad (53)$$

$$\dot{x}_{28} = -\frac{1}{a_{68}a_{69}} x_{28} - \frac{1}{a_{68}(a_{66}+a_{67})} * (V_{oc} + x_{29} + x_{30} - x_{27}) \quad (54)$$

$$\dot{x}_{29} = -\frac{1}{a_{72}a_{73}} x_{29} + \frac{1}{a_{72}(a_{66}+a_{67})} * (V_{oc} + x_{29} + x_{30} - x_{27}) \quad (55)$$

$$\dot{x}_{30} = -\frac{1}{a_{74}a_{75}} x_{30} + \frac{1}{a_{74}(a_{66}+a_{67})} * (V_{oc} + x_{29} + x_{30} - x_{27}) \quad (56)$$

$$\dot{\xi}_{14} = r_{10} - \frac{(x_5 - x_{26})}{a_{64}} \quad (57)$$

$$d_{12} = a_{75}\left(r_{10} - \frac{(x_5 - x_{26})}{a_{72}}\right) + a_{76}\xi_{14} \quad (58)$$

III. CASE STUDIES WITH THE COMPREHENSIVE MODEL

Several case studies have been conducted with the developed comprehensive FREEDM system model to evaluate the impact on the output voltage levels in different stages of the system and track performance for the controller set-points. Results are observed where DC and AC buses are maintained at the set voltage levels with load changes in DC or AC energy cells, start/stop of DRER generation and DESD charging/discharging modes. Summary results of two particular cases are shown in Fig. 9. Fig. 9(a) shows that PV generation of 0.5 kW added at t=1 sec from the DC energy cells causes an overshoot in the SST rectifier and DAB output voltages with energy being fed back to the grid. The energy storage in the charging mode and wind generation unit are connected to the system at t=2 secs and 3.2 secs, respectively. The DC voltage in rectifier and DAB output drops at first, but the controllers are able to maintain the steady-state regulation. For analyzing the dynamics introduced by the AC energy cell, PV DRER, AC DESD, and wind generation are connected to the system at t=5 secs, 6 secs and 7.2 secs, respectively. Fig. 9(b) shows that the DC bus voltage fluctuates due to addition of the AC energy cell components. The AC output voltage fluctuations, which are smaller, can only be seen when decomposed to *d-q* axes. Fig. 10 shows the system response when the SST operating mode is changed for reversing the power flow with renewable generation and active load reduction. DC bus voltage of the rectifier and DAB show overshoot before settling to the desired regulation points within 0.3 secs.

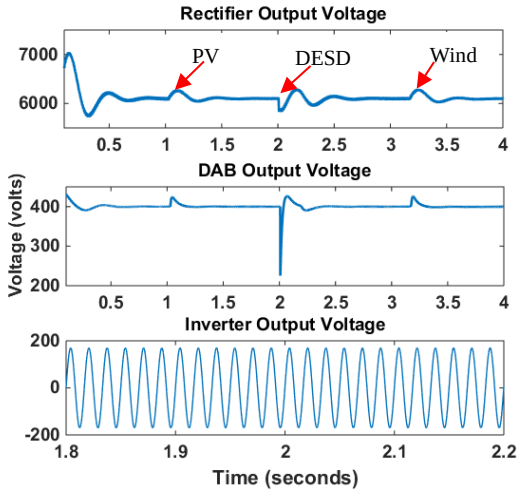

(a)

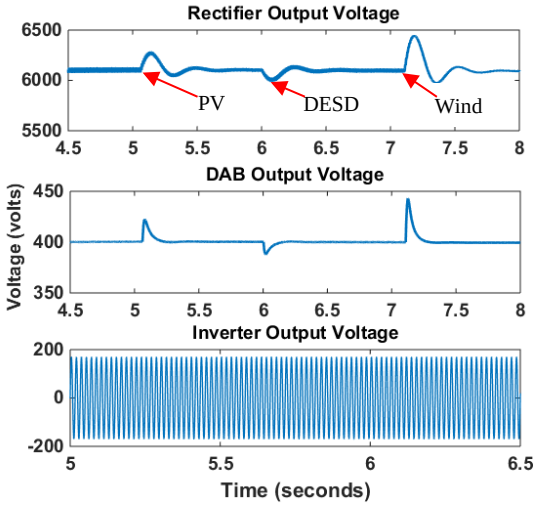

(b)

Figure 9: Case studies with 70th order average model.

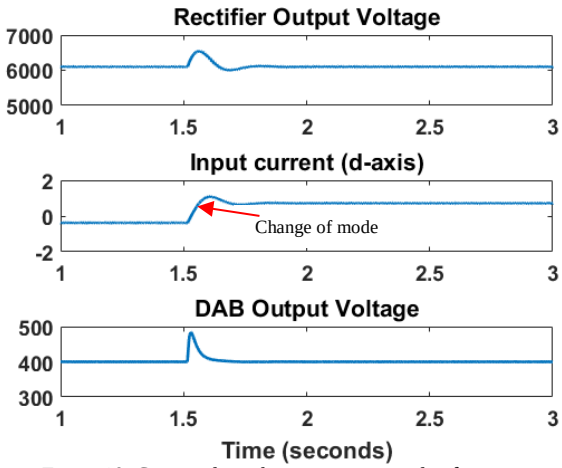

Figure 10: Case study with regenerative mode of operation.

Fig. 11 shows the system response following a 30% voltage sag in the grid voltage from 3.6 kV to 2.52 kV. The controller is able to regulate the output voltage of rectifier, DAB and inverter with the change in input voltage at t=2 secs. As the DC voltages are regulated precisely, the impact on the inverter output voltage is minimal with grid voltage variations.

The system response with variations in output DC load has also been analyzed with the model. Fig. 12 shows the response of the regulated voltages after a step change in DC load from 50 ohms to 80 ohms. The controller is able to regulate the output voltage of rectifier, DAB and inverter with the 60% change in active power at t=2 secs. DAB voltage shows a 10% surge due to the step change, but it settles to the regulated voltage of 400 V within 0.15 secs.

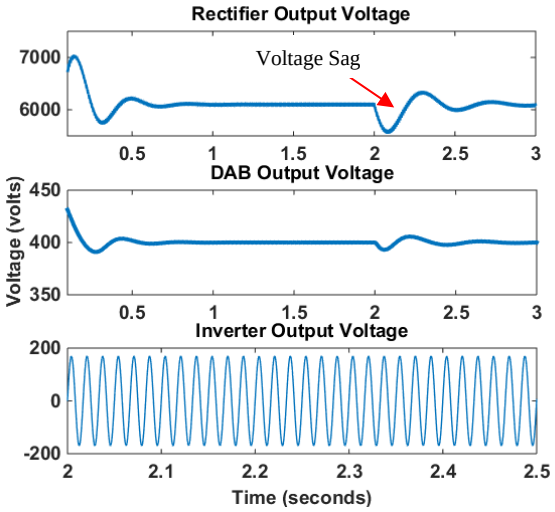

Figure 11: Case study with input voltage variation.

The robustness of the controller with respect to parameter variation has been verified by changing the filter resistance to observe the impact of physical parameters on controllers. Fig. 13 shows the response of the regulated voltage after a step change in input filter resistance of the rectifier from base value of 47 ohms to 80 ohms. The controller is able to regulate the output voltage of rectifier, DAB and inverter with the change in system parameter values at t=2 sec. The rectifier output voltage shows a transient value of less than 0.10% due to the step change; the inverter voltage does not have any noticeable transient. This analysis further shows that the transient voltage responses do not show any significant overshoot/undershoot even with parameter variations up to 80% from base values. It has been found that the rectifier filter resistance determines the feasible operation region of the system which will be further explained in the next section.

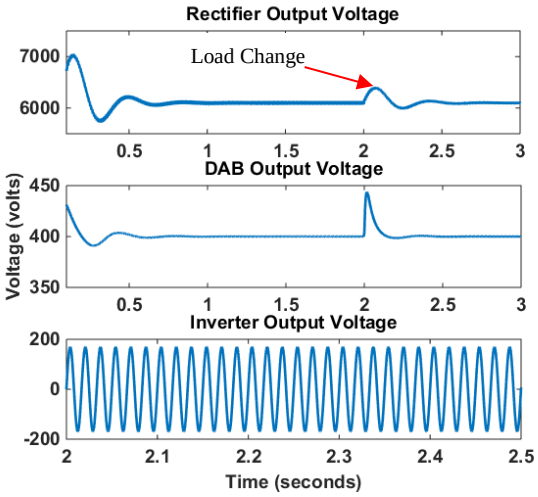

Figure 12: Case study with active power variation.

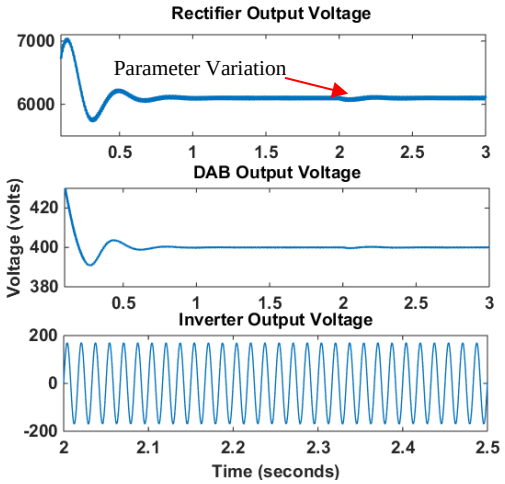

Figure 13: Case study system parameter variation.

IV. FREEDM SYSTEM FEASIBILITY ANALYSIS

The nonlinear differential-algebraic state-space model of a single-SST FREEDM power distribution system developed in the previous sections provides the opportunity to derive analytical relationships between physical parameters and feasible operational range of the system. Feasible operation range based on the physical parameters is critical for a continuous system operation and feasibility analysis of the FREEDM system is essential to answer the maximum net power capability that the system can handle. Once the feasibility bounds are known, the system parameters can be designed in hardware accordingly to provide the required power flow and energy exchange flexibility. The pair (y_1, I_{DAB}) has been identified to be critical for determining the equilibrium of the nonlinear FREEDM model where I_{DAB} represents the net current flowing through the DAB stage of the SST and y_1 is the d-axis grid voltage. Existence and uniqueness of equilibrium are analyzed utilizing the rectifier state equations (1-8) as

other parts of the FREEDM system can be lumped as an output load in the rectifier. Initially, steady state value for the *d*-axis grid current is found, and then, necessary conditions for I_{DAB} to maintain feasibility of SST is derived which is shown in equations (59-60).

$$x_{1,ss} = \frac{-\frac{y_1}{a_2} \pm \sqrt{(\frac{y_1}{a_2})^2 - \frac{8I_{DAB,ss}r_2}{a_2}}}{2} \quad (59)$$

$$I_{DAB,ss} \leq \frac{y_1^2}{8a_2r_2} \quad (60)$$

Fig. 14 shows the relationship between the system parameters and controller gains with the feasibility and stability region. In each subfigure, for a given set of (y_1, I_{DAB}) in a range, it has been found if that operating point is infeasible (white), feasible and stable (green) or feasible and unstable (red). As it can be seen, decreasing the filter resistance has resulted in reduction of the white space which means that the feasible operation region has expanded. Moreover, the analysis has been done based on a nominal set of controller parameters used in the case studies of section III. By tuning the controller parameters from G_i *to* G_j, it is possible to reduce the region of unstable points. G_0 is the nominal controller and G_1, G_2 are the tuned controllers to improve the stability of the system based on eigenvalue analysis in the linearized rectifier model. However, the important point to consider is that the infeasible region of the system will not change by tuning the controllers as the white zone remains unchanged after tuning the controller gains. The results are graphically shown in Fig. 15 and Fig. 16.

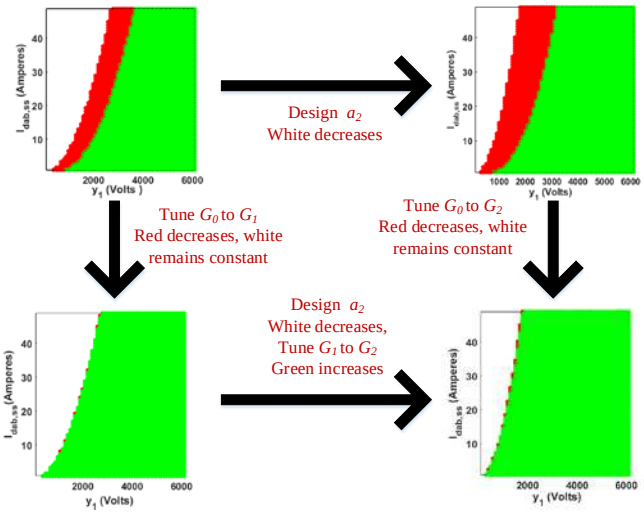

Figure 14. Feasibility and stability circle diagram.

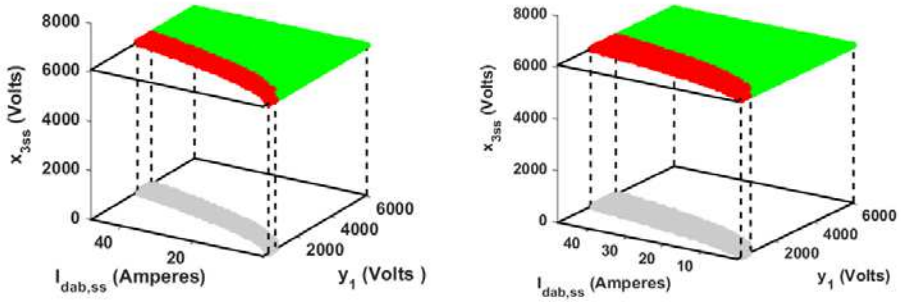

(a) (b)

Figure 15. Expansion of feasibility region by reducing rectifier resistance from (a) to (b).

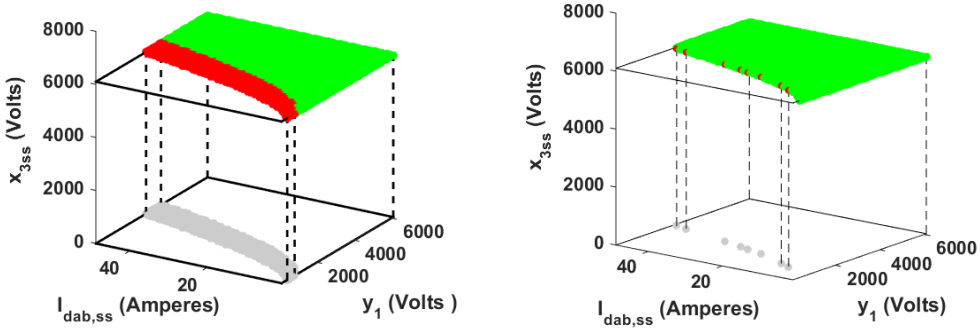

(a) (b)

Figure 16. Expansion of stability region by retuning the controller gains (a) to (b).

Rectifier input filter resistance (a_2) can be designed to provide expanded feasible operation region for any pair of (y_1, I_{DAB}). Fig. 15 shows that reducing a_2 results in expansion of feasible operating region of SST. Red zones represent the unstable regions inside the feasible operational range which can be reduced with the proper tuning of the controller gains. Fig. 16 presents a particular case of the controller tuning to show the expansion of the stable region. However, with the tuning of the controller, the white region does not change that indicates the failure due to the feasibility bounds is not dependent on controller design.

V. FEASIBILITY ANALYSIS IN A SYSTEM SIMULATION TESTBED

The comprehensive single-SST average model has been incorporated in an IEEE 34 bus large scale system simulation (LSSS) testbed in a PSCAD platform with multiple SSTs for a scaled analysis of the system. The developed multi-SST simulation model is used to find the feasible operating bounds of the system considering the coupling and interaction among multiple SSTs in the distribution system. The LSSS testbed shown in Fig. 17 has 26 nodes where each node has one or more SSTs in different phases with the configuration shown in Fig. 2. There are a total of 40 SSTs connected in the various nodes of the LSSS testbed. In this LSSS testbed, only PV DRER is considered. Simulation analysis has been carried out to validate the feasibility conditions analyzed in the previous section through analytical means.

Fig. 18 presents the simulation analysis results for the nearest (806), middle (820) and farthest (840) feeders from the point of common coupling (PCC) in Fig. 17. SST input voltage (*d*-axis) and rectifier output voltages of the three feeders are shown in Fig. 18 as representative system variables. The rectifier output voltage in feeder 806 is being regulated at its desired value of 6100 V; the small variations are due to the changes of DRER and DESD currents into the system. The rectifier output voltage for the mid-network feeder 820 shows higher levels of dynamic variations due to the current changes in the DRERs and DESDs.

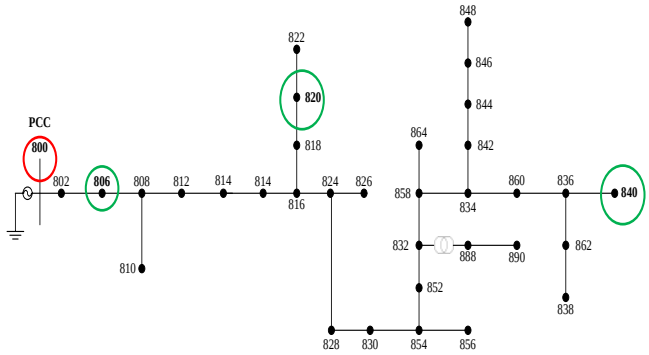

Figure 17: LSSS testbed with circled nodes whose analysis results are presented in Figs. 18 and 19.

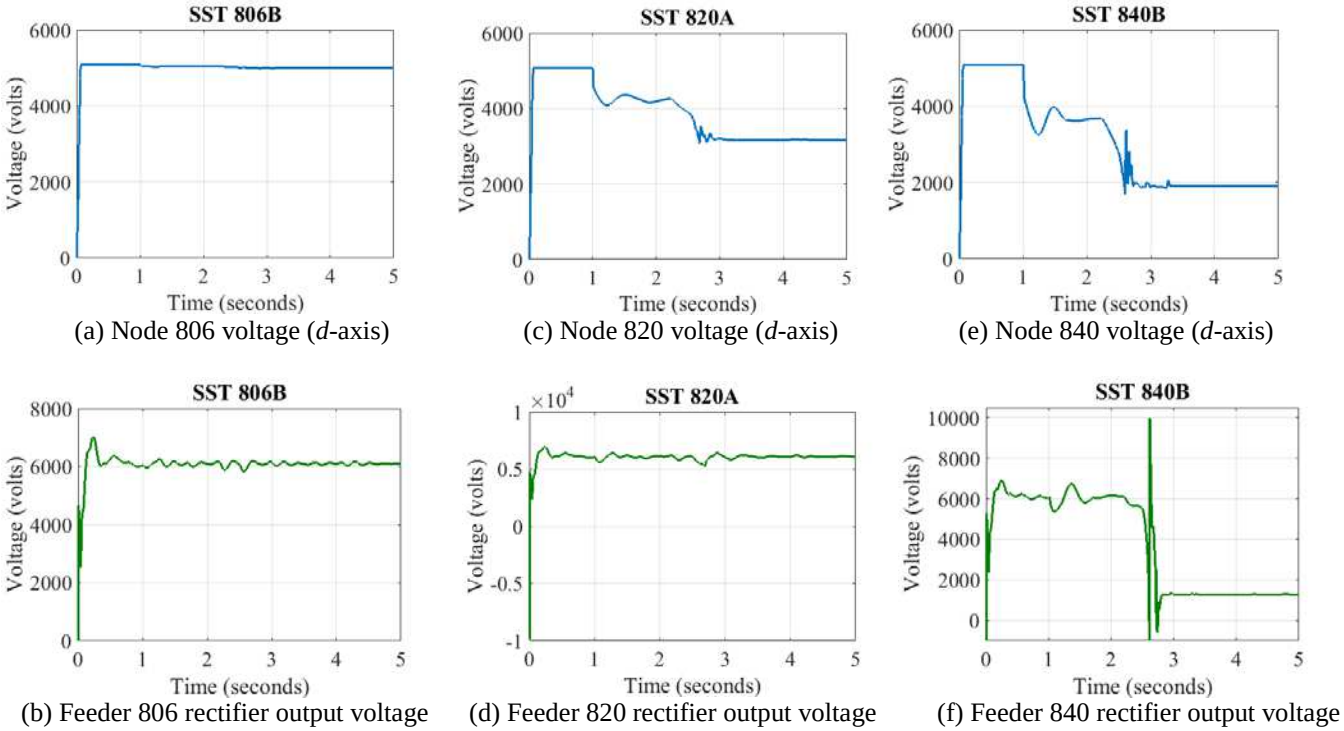

(a) Node 806 voltage (*d*-axis) (c) Node 820 voltage (*d*-axis) (e) Node 840 voltage (*d*-axis)

(b) Feeder 806 rectifier output voltage (d) Feeder 820 rectifier output voltage (f) Feeder 840 rectifier output voltage

Figure 18: Feasibility analysis for SST in IEEE 34 bus.

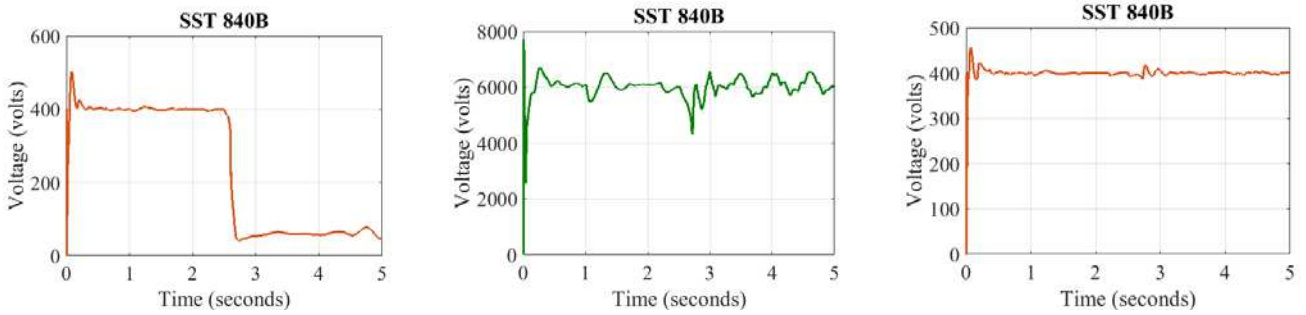

(a) Feeder 840 DAB output voltage before change in resistance

(b) Feeder 840 rectifier output voltage after change in resistance

(c) Feeder 840 DAB output voltage after change in resistance

Figure 19: Failure analysis for distant SST in IEEE 34 bus.

Although the rectifier input voltage decreases, the net load for the SST at node 820 is still within the feasibility bound, and hence, it does not fail. The results for the farthest feeder 840 shows that the input voltage keeps decreasing, and at 2.5 secs the operation fails when the voltage reaches a level that is lower than that required to maintain feasible operation. The failure at feeder 840 is due to the violation of feasibility constraint as the net load in the system (~20 kW/ 50 amps) is more than the system can handle (~10.2 kW/ 25.5 amps) with the reduced input voltage. The results show that the feeder which is farthest from the grid suffers from infeasibility due to voltage loss in the feeder network. As the voltage level decreases at distant nodes, the maximum current that can be drawn by the DAB stage exceeds the limits forcing the SST to enter an infeasible operating region.

To study the effect of parameter values on system feasibility, the rectifier filter resistance has been reduced by one-third to increase the feasibility range (~30 kW/ 80 amps) with the same voltage level. Fig. 19 (a) shows the results for the DAB voltage before the resistance is changed which fails to maintain the desired set point of 400 V. Fig. 19 (b) and Fig. 19 (c) show that the rectifier and DAB output voltages with changed resistance value are regulated and the system is within the feasibility range with node voltage as in Fig. 18 (e) and similar net load. The controller gains need to be further tuned to reduce the dynamic variations seen in the output voltages.

The key parameters affecting the feasibility range of a multi-SST power distribution system can be obtained with the presented models and analysis. The results from the nonlinear simulation model correlate well with the results seen earlier in the surface plots. The parameters can be tuned appropriately in the design stage to enhance the feasibility region, and also to determine the operation bounds needed for controller design. A similar approach for design and analysis can be used for any physical hardware used in traditional microgrid. The operation bounds provide the critical information on when system will fail due to feasibility violation rather than because of a controller instability issue. The models developed in this work have been used for equilibrium analysis and power sharing algorithm development for a multi-SST system in [21].

VI. Conclusions and Future Work

Feasibility of a solid-state transformer based FREEDM power distribution system is analyzed following the development of a 70th-order state-space system representation of a FREEDM system node. Detailed SST model along with renewable generation and storage systems and their corresponding interface circuits to DC and AC buses are considered in the modeling. The model is then used to define the feasible operational bounds for the FREEDM system, which is required for ensuring power balance in the multi-SST FREEDM system where strong coupling and interaction exist among various system components. Satisfying the feasibility conditions in the multi-SST FREEDM system is a necessary condition for system stability independent of the performance of the local SST power management controllers.

An IEEE 34 bus power distribution LSSS testbed has been developed to analyze the feasibility constraint and the power and energy sharing capability of the energy cells in a multiple-SST connected FREEDM system. The feasibility analysis results in the large scale simulation testbed demonstrate the dependence of system feasibility on rectifier filter resistance which was also observed in the linearized model analysis. The feasibility analysis helps selected the appropriate filter resistance based on the SST location in the distribution feeder. In a multi-SST system (which is similar to multiple power electronic converters connected in a network), there are two fundamental reasons for instability, one is system power imbalance among sources and sinks leading to infeasible zones of operation, and the second is the harmonic resonance between converter controller and the network impedance. The developed comprehensive model provides the platform for feasibility analysis, design guidance for system parameter selection, and controller evaluation.

ACKNOWLEDGMENT

This work was supported by ERC program of National Science Foundation under award number EEC-0812121 for the FREEDM Engineering Research Center.

REFERENCES

[1] A. Q. Huang, M. L. Crow, G. T. Heydt, J. P. Zheng and S. J. Dale, "The Future Renewable Electric Energy Delivery and Management (FREEDM) System: The Energy Internet," in *Proceedings of the IEEE*, vol. 99, no. 1, pp. 133-148, Jan. 2011.

[2] X. She, X. Yu, F. Wang and A. Q. Huang, "Design and Demonstration of a 3.6-kV–120-V/10-kVA Solid-State Transformer for Smart Grid Application," in *IEEE Transactions on Power Electronics*, vol. 29, no. 8, pp. 3982-3996, Aug. 2014.

[3] S. Bhattacharya *et al.*, "Design and Development of Generation-I Silicon Based Solid State Transformer," *2010 Twenty-Fifth Annual IEEE Applied Power Electronics Conference and Exposition (APEC)*, Palm Springs, CA, 2010, pp. 1666-1673.

[4] T. Zhao, L. Yang, J. Wang and A. Q. Huang, "270 kVA Solid State Transformer Based on 10 kV SiC Power Devices," *2007 IEEE Electric Ship Technologies Symposium*, Arlington, VA, 2007, pp. 145-149.

[5] E. R. Ronan, S. D. Sudhoff, S. F. Glover and D. L. Galloway, "A Power Electronic-Based Distribution Transformer," in *IEEE Transactions on Power Delivery*, vol. 17, no. 2, pp. 537-543, Apr 2002.

[6] G. G. Karady, A. Q. Huang and M. Baran, "FREEDM System: An Electronic Smart Distribution Grid for The Future," *PES T&D 2012*, Orlando, FL, 2012, pp. 1-6.

[7] V. Ramachandran, A. Kuvar, U. Singh, S. Bhattacharya, M. E. Baran, "A System Level Study Employing Improved Solid-State Transformer Average Models with Renewable Energy Integration," *in PES General Meeting Conference & Exposition*, 2014 IEEE, pp.1-5, 27-31 July 2014.

[8] T. Zhao, J. Zeng, S. Bhattacharya, M. E. Baran, and A. Q. Huang, "An Average Model of Solid State Transformer for Dynamic System Simulation," *in Proc. IEEE Power Energy Soc. Gen. Meeting*, Jul. 2009, pp. 1–8.

[9] Z. Yu, R. Ayyanar, I. Husain, "A Detailed Analytical Model of A Solid-State Transformer," *in Energy Conversion Congress and Exposition (ECCE)*, 2015 IEEE, pp.723-729, 20-24 Sept. 2015.

[10] Y. Jiang, L. Breazeale, R. Ayyanar, and X. Mao, "Simplified Solid State Transformer Modeling for Real Time Digital Simulator (RTDS)," *Energy Conversion Congress and Exposition (ECCE)*, 2012 IEEE, pp. 1447– 1452, Sept 2012.

[11] X. Yu, X. She, X. Ni and A. Q. Huang, "System Integration and Hierarchical Power Management Strategy for a Solid-State Transformer Interfaced Microgrid System," in *IEEE Transactions on Power Electronics*, vol. 29, no. 8, pp. 4414-4425, Aug. 2014.

[12] D. G. Shah and M. L. Crow, "Stability Design Criteria for Distribution Systems With Solid-State Transformers," in *IEEE Transactions on Power Delivery*, vol. 29, no. 6, pp. 2588-2595.

[13] J. W. Kimball and P. T. Krein, "Singular Perturbation Theory for DC– DC Converters and Application to PFC Converters," *in Proc. IEEE Power Electron. Spec. Conf.*, Orlando, FL, 2007, pp. 882–887.

[14] M. T. A. Khan, A. A. Milani, A. Chakrabortty and I. Husain, "Comprehensive Dynamic Modeling of A Solid-state Transformer Based Power Distribution System," *in Energy Conversion Congress and Exposition (ECCE)*, IEEE, Sept. 2016.

[15] F. Wang, G. Wang, A. Huang, W. Yu and X. Ni, "Design and Operation of A 3.6kV High Performance Solid State Transformer Based on 13kV SiC MOSFET and JBS Diode," *2014 IEEE Energy Conversion Congress and Exposition (ECCE)*, Pittsburgh, PA, 2014, pp. 4553-4560.

[16] H. Bai, C. Mi, C. Wang, and S. Gargies, "The Dynamic Model and Hybrid Phase-Shift Control of A Dual-Active-Bridge Converter," *in Proc. 34th Annu. IEEE IECON*, Nov. 2008, pp. 2840–2845.

[17] M. G. Villlalva, J. R. Gazoli, and E. Ruppert, "Comprehensive Approach to Modeling and Simulation of Photovoltaic Arrays," *IEEE Trans. Power Electron.*, vol. 24, no. 5, pp. 1198–1208, May 2009.

[18] Shengyi Liu and R. A. Dougal, "Dynamic Multiphysics Model for Solar Array," in *IEEE Transactions on Energy Conversion*, vol. 17, no. 2, pp. 285-294, Jun 2002.

[19] Z. M. Salameh, M. A. Casacca, and W. A. Lynch, "A Mathematical Model for Lead-Acid Batteries," *IEEE Trans. Energy Convers.*, vol. 7, no. 1, pp. 93–98, Mar. 1992.

[20] Min Chen and G. A. Rincon-Mora, "Accurate Electrical Battery Model Capable of Predicting Runtime and I-V Performance," in *IEEE Transactions on Energy Conversion*, vol. 21, no. 2, pp. 504-511, June 2006.

[21] A. Afiat Milani; M. T. A. Khan; A. Chakrabortty; I. Husain, "Equilibrium Point Analysis and Power Sharing Methods for Distribution Systems Driven by Solid-State Transformers," in *IEEE Transactions on Power Systems* , vol.PP, no.99, pp.1-1.